EDTA as chelating agent for sol-gel synthesis of spinel LiMn 2 O 4 cathode material for lithium batteries

A. M Hashem, A. Abdel-Ghany, H. M Abuzeid, R S El-Tawil, S. Indris, H. Ehrenberg, A. Mauger, C.M. Julien

EDTA as chelating agent for sol-gel synthesis of spinel $LiMn_2O_4$ cathode material for lithium batteries

A. M. Hashem[1,2] A. E. Abdel-Ghany[1], H. M. Abuzeid[1], R. S. El-Tawil[1], S. Indris[2], H. Ehrenberg[2], A. Mauger[3], C. M. Julien[3,*]

[1]National Research Centre, Inorganic Chemistry Department, 33 El Bohouth St., (former El Tahrir St.), Dokki-Giza 12622, Egypt

[2]Karlsruhe Institute of Technology (KIT), Institute for Applied Materials (IAM), P.O. Box 3640, 76021 Karlsruhe, Germany

[3]Sorbonne Universités, UPMC Univ. Paris6, Institut de Minéralogie, de Physique des Matériaux et de Cosmochimie (IMPMC), UMR 7590, 4 place Jussieu, 75005 Paris, France

***Corresponding author**: e-mail: Christian.julien@upmc.fr

Abstract

Ethylene diamine tetra-acetic acid (EDTA) was used to prepare spinel $LiMn_2O_4$ at 650 °C. The prepared sample by EDTA (E-$LiMn_2O_4$) is compared with another spinel sample (C-$LiMn_2O_4$) prepared by citric acid as a common chelating agent at the higher temperature (800 °C) adjusted to obtain the same size and shape of the particles as in (E-$LiMn_2O_4$) sample, as probed by SEM and TEM images. Investigation of both samples by X-ray diffraction showed that both samples have the single phase cubic spinel $LiMn_2O_4$ phase with space group *Fd*-3*m*. Vibration properties obtained from Raman scattering (RS) and Fourier Transform Infra-Red (FTIR) spectroscopy for both samples are identical with spinel $LiMn_2O_4$ structure. ^{7}Li MAS NMR and XPS spectra show that the amount of Mn^{4+} is larger in $LiMn_2O_4$ sample prepared by citric acid. $LiMn_2O_4$ sample prepared using EDTA as chelating agent has better structural properties, but the improvement of the electrochemical properties is much smaller than the results reported in the literature for lamellar compounds and silicate materials. This is attributed to the features specific to the spinel, which limit both the capacity and cycle ability: dissolution of manganese and Jahn-Teller distortions associated to Mn^{3+} ions, that are not modified by the choice of chelating agent.

Keywords: Lithium-ion batteries; cathode material; spinel structure; sol-gel synthesis, EDTA.

1. Introduction

Nano-materials with controllable size and shape have received enormous attention due to their promising applications in various fields, such as catalysis, gas sensing and batteries [1]. Rechargeable lithium ion batteries (LIBs) have drawn extensive attention as the most promising candidates to power the next generation of electric vehicles and electronic equipment due to their high-energy density, high working voltage, low self-discharge rate, long shelf life [2]. The various commercialized Li-ion batteries mainly differ by the chemistry of the active cathode material, which then plays a key role in the determination of both their energy and their cost. Currently, lithium cobalt oxide ($LiCoO_2$), which is known for its high-energy density and good cycling stability, is the most commercialized cathode material for LIBs. However, the high price and toxicity of cobalt have prevented its use in next-generation LIBs [3]. Spinel-type $LiMn_2O_4$ oxide (LMO), which has three-dimensional lithium diffusion paths is considered as one of the most promising alternative cathode materials for LIBs due to the advantages such as good environmental compatibility, good thermal stability, its abundant raw material resources, low production cost, high potential plateau, and good safety [4]. However, its capacity fading during cycling, especially at high temperature, restricts its commercial usage for rechargeable Li-ion batteries [5]. Generally, current commercial $LiMn_2O_4$ products can reach 100–120 mAh g^{-1} while the theoretical capacity is 148 mAh g^{-1} [6]. Many efforts are currently made in research to improve the capacity of $LiMn_2O_4$ and its cycling life. In the present work, we report on different synthesis conditions in order to optimize the synthesis parameters leading to the best electrochemical properties of $LiMn_2O_4$. Commercial spinel $LiMn_2O_4$ is synthesized by a high temperature solid-state reaction, which has advantages of facile synthesis and large-scale production. On another hand, it also has several disadvantages such as non-homogeneities, irregular morphology, long calcination times and slow reaction kinetics. Consequently, the formation of pure single-phase product is hindered, and the process leads to the formation of larger particles with broad particle size distribution. It also impedes the Li-ion diffusion into the cathode [7], which affects the rate capability [8]. Therefore, the reduction of the size of the particles is desirable in order to increase the performance at high rate of charge and discharge by reducing the length of the path for electrons and Li^+ ions within the $LiMn_2O_4$ particles, and by increasing the effective surface area [9-10].

To overcome these disadvantages and prepare particles of smaller size, many wet-chemical methods are being used, which include micro-emulsion [11-12], hydrothermal synthesis [13], sol–gel [14], microwave-induced combustion [15], and spray drying method [16].

Zhang et al. have outlined the fact that the electrochemical performance of α-MnO_2 strongly depends on the synthesis procedure, i.e. chelating agent used in the wet-chemical method [17]. Actually, this exemplifies the role of the chelating agent that is important in any synthesis process. The choice of ethylene diamine tetra-acetic acid (EDTA), which is an aminopolycarboxylic acid and water-soluble solid, forms complex precursor for a low temperature synthesis of cathode materials; it has proved to be efficient to improve the properties of the $LiCoO_2$ cathode already 15 years ago [18]. Since then, it has also been used to synthesize $Li_{1-x}K_xCoO_2$ [19]. A sol-gel synthesis of Li_2MnO_3 and $Li[Li_{0.2}Mn_{0.6}Ni_{0.2}]O_2$ by a combined EDTA and citric acid complexation route has also been successful [20]. Recently, an EDTA-sol-gel method has been used to synthesize LiV_3O_8 [21]. A comparative study of the electrochemical properties of $LiNi_{0.80}Co_{0.15}Al_{0.05}O_2$ cathode synthesized by sol-gel method with different complexing agents (EDTA, glycine and citric acid) shows that the best structural properties, the largest capacity and the best cycle ability were obtained with EDTA [22]. The beneficial effect of EDTA on lamellar compounds outlined in these works has also been tested on $Li_3V_2(PO_4)_3$/C composite [23]. This complexing agent has been rarely used for the synthesis of the $LiMn_2O_4$. We found a report of this synthesis in [24], but the electrochemical properties were not explored.

In the present work, a wet chemistry method at moderate temperature and short time using EDTA and citric acid as chelating agents have been used to explore the best conditions to produce nanoparticles of $LiMn_2O_4$ to optimize the electrochemical properties of this cathode material for lithium-ion batteries. Compared with the conventional wet-chemical method, the EDTA assisted sol-gel process offers many advantages such as a better control of material morphology and better electrochemical performance.

The recent progress of $LiMn_2O_4$ has been obtained by surface modifications of the nanoparticles to prevent the manganese from dissolution in the electrolyte containing acidic species. A review of these modifications can be found in [25]. In this work, Lee et al. reported a novel heterostructure with epitaxially grown *R*-3*m* surface phase. This result shows that there are now coating layers that satisfy the requirement of chemical affinity between the host and the surface layer to solve the problem that limited the use of $LiMn_2O_4$ in different applications,

including electric vehicle. We thus believe that the cheap and easy mode of preparation of $LiMn_2O_4$ that can benefit of such surface modifications is promising to promote this material in the industry, without the need of less scalable and expensive syntheses process involving hollow nanofibers with a porous structure by modified electrospinning techniques and subsequent thermal treatment [26], or by doping with rare earths [27].

2. Experimental

To compare the effect of the chelating agent, two $LiMn_2O_4$ samples were prepared by sol–gel process using citric acid and EDTA as chelating agents. $LiMn_2O_4$ powders were prepared using appropriate molar ratios of lithium and manganese acetate dissolved in distilled water. Carboxylic acids, such as citric acid and EDTA, act as fuel during the formation process of transition-metal oxide powders, and they decompose the homogenous precipitate of metal complexes at temperature T<450 °C. The dissolved solution was added dropwise to a continuously stirred aqueous solution of chelating agent. The molar ratio between metal and chelating agent was adjusted to be 1:1. The COOH group of chelating agent forms a chemical bond with the metal ions and, after evaporation of the solvent by heating the prepared solution at 80 °C with magnetic stirring for about 6 h, a transparent xerogel was obtained. This gel precursor was decomposed at 450 °C for 4 h in air to eliminate the organic substances and cooled to room temperature. The decomposed powders were slightly ground using a mortar and calcined in air for 12 h at 600 and 800 °C for EDTA and citric acid, respectively. In the following, the corresponding products are named E-$LiMn_2O_4$ and C-$LiMn_2O_4$, respectively.

The crystal structure of $LiMn_2O_4$ samples was analyzed by X-ray diffraction (XRD) using a Philips X'Pert apparatus equipped with a Cu Kα X-ray source (λ = 154.06 pm). XRD data were collected in the 2θ range 10–80° at room temperature. Raman spectra have been recorded in spectral range 200-800 cm^{-1} at room temperature in a quasi-backscattering geometry. A double monochromator (Jobin-Yvon model U1000) with holographic gratings and a computer-controlled photon-counting system was used. The laser light source was the 514.5nm line radiation from a Spectra-Physics 2020 argon-ion laser. To have a large signal to noise ratio, 12 successive scans recorded at a spectral resolution of 2 cm^{-1} are averaged. FTIR spectra were recorded using a Bruker model IFS113v interferometer equipped with a MCT mid-IR and

DTGS/PE detectors. Specimens were prepared by the disk method using powders mixed with CsI (1:300) and pressing them at 5 tons cm^{-2} with good transparency for IR radiation. A JEOL, Transmission Electron Microscope (TEM, JEM-1230, Japan) was used to investigate the prepared sample. ^{7}Li MAS NMR spectra were measured with a Bruker Avance 200 MHz spectrometer with a magnetic field of 4.7 T corresponding to a Larmor frequency of 77.8 MHz. Spinning was performed in 1.3 mm rotors at 60 kHz. Spectra were acquired with a rotor-synchronized Hahn-echo pulse sequence ($\pi/2$-τ-π-τ-acq.) and chemical shifts are given relative to that of a 1 mol L^{-1} LiCl aqueous solution. The $\pi/2$ pulse length was 1.4 μs and the recycle delay was 1 s. X-ray photoelectron spectroscopy (XPS, PHI 5800 apparatus with a monochromatic Al Kα (1486.6 eV) anode (250 W, 10 kV, 27 mA)) was used in evaluating the chemical state of Mn cations.

$LiMn_2O_4$ electrode was prepared by mixing 80% (w/w) of the active material, 10% (w/w) super C65 carbon (TIMCAL) and 10% (w/w) polyvinylidenefluoride (Solef PVdF 6020 binder, Solvay) in N-methyl-2-pyrrolidone (NMP, Sigma-Aldrich) to get a slurry. The cathode loading of 2 mg cm^{-2} was obtained with a 90 μm thin film coated on aluminum foil. This film was dried over night at 80 °C then electrodes were punched out with the diameter of 1.2 cm. After subsequent drying at 100 °C under vacuum, this electrode film was finally pressed at 8 tons. The cell was assembled using the two electrode Swagelok®- type test cells in an argon-filled glove box with lithium foil (Alfa Aesar) as anode, LP30 (1M $LiPF_6$ in ethylene carbonate (EC):dimethylcarbonate (DMC)1:1) as electrolyte and glass microfiber filters (Whatmann®-GF/D 70 mm Ø) as separator. A VMP3 multi-channel potentiostat (Bio-Logic, France) was used to electrochemically characterize the electrodes at 25 °C in the voltage range of 3.0-4.5 V with galvanostatic cycling and cyclic voltammetry (CV) techniques.

3. Results and discussion

3.1. Structural properties

XRD patterns for $LiMn_2O_4$ synthesized by sol-gel method using citric acid and EDTA as chelating agents at calcination temperatures of 800 and 600 °C, respectively, are shown in Fig.1a. All the diffraction peaks of the two samples are indexed according to the single phase cubic spinel phase with *Fd*3*m* (O_7^h) space group [7] (JSCD No. 050427 card). The lattice

parameters were calculated via a least-squares refinement method using 10 well-defined diffraction lines with indexation in the cubic system and the results are summarized in Table 1. The main diffraction peaks are (111), (311) and (400), as expected for the spinel phase. It means that the lithium ions occupy the tetrahedral (8*a*) sites (Wyckoff notation) and manganese ions are distributed at octahedral (16*d*) sites, while oxygen anions are located at the (32*e*) sites [4,28]. No impurities such as Li_2MnO_3, $LiMnO_2$, Mn_2O_3 or MnO_x were detected, which gives evidence of the high purity of the synthesized products. The sharpness of main peaks indicates that both samples are well crystallized [29]. However, the peak intensity and the full-width at half-maximum (FWHM) are different for C- and E-$LiMn_2O_4$, which indicates a difference in crystallinity, particle size and ordering of local structure between the two samples. This difference can be evidenced by the use of the Scherrer formula [31]:

$$B^2\cos^2\theta = 16e^2\sin^2\theta + \frac{K^2\lambda^2}{L^2} \quad (1)$$

where B is the FWHM, θ is the diffraction angle, $\langle e^2 \rangle$ denotes local strains (defined as $\Delta d/d$ with d the interplanar spacing), L is the crystallite size and K =0.88 for a spherical crystallite shape. The plot of $B^2\cos^2\theta$ as a function of $\sin^2\theta$ is reported in Fig. 1b for C- and E-$LiMn_2O_4$ samples. The slope, $16\langle e^2 \rangle$, and intercept $K^2\lambda^2/L^2$, were used to estimate the strain $\langle e^2 \rangle$ and coherence length L respectively (Table 1). We find that the crystallite is larger and the strain field smaller in the E-$LiMn_2O_4$ sample. Therefore, we find that the result obtained for lamellar and silicate compounds according to which EDTA leads to better structural properties than the citric acid also applies to the $LiMn_2O_4$ spinel. This property is usually attributed to the fact that the calcination temperature is smaller when EDTA is used as chelating agent. In the present case, however, an additional improvement is a modification of the valence mixing of manganese ions ($Mn^{3+}$and Mn^{4+}). Since the ionic radius of Mn^{4+} (0.53 Å) is smaller than that of Mn^{3+} (0.645 Å), the *"a"* lattice parameter decreases when the Mn^{3+}/Mn^{4+} ratio decreases, ranging from 8.2104 Å to 8.2446 Å between $Li_{0.76}Mn_{1.65}O_4$ and $Li_{1.055}Mn_{1.993}O_4$, respectively [32]. A similar lattice shrinkage associated to a decrease of the amount of Mn^{3+} has been observed for Y^{3+} substitution [33] and Nd^{3+} substitution [34] for Mn^{3+} in $LiMn_2O_4$. The value of a=8.2311(1) Å in the E-$LiMn_2O_4$ is the value expected for stoichiometric $LiMn_2O_4$ [31] and we can estimate that the average valence for this sample is +3.5. Note that the much larger error ±0.007 Å in the determination of the lattice parameter of sample C-$LiMn_2O_4$ makes difficult the estimation of the

deviation from stoichiometry if any. Actually, this larger error is another evidence of the stronger local disorder of the lattice in this sample.

Table 1. XRD Parameters for $LiMn_2O_4$ materials synthesized by wet chemistry assisted citric acid and EDTA.

Sample	*a* (Å)	*V* (Å^3)	$<e^2> *10^{-6}$	*L* (nm)
E-$LiMn_2O_4$	8.2311(1)	557.9	1.57	131
C-$LiMn_2O_4$	8.239(7)	561.1	2.14	123

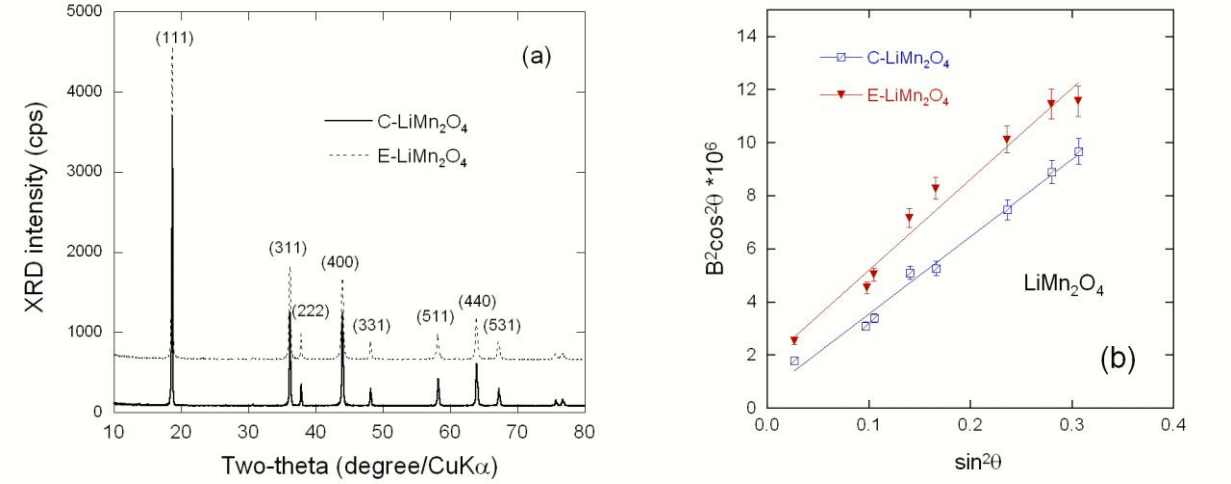

Fig. 1 (a) XRD diffraction patterns of C-$LiMn_2O_4$ and E-$LiMn_2O_4$. (b) Analysis of the fullwidth at half maximum *B* of the Bragg peaks.

SEM and TEM images of as-synthesized $LiMn_2O_4$ samples using citric acid (C-$LiMn_2O_4$) and EDTA (E-$LiMn_2O_4$) are displayed in Figs. 2 and 3, respectively. Both the C- and E-$LiMn_2O_4$ particles have a size in the range of 300-400 nm. It implies that the difference in the calcination temperature used in the two synthesis processes did not affect neither the shape nor the size of the particles, so that the differences between the electrochemical properties of these two cathode materials will be solely attributable to structural properties.

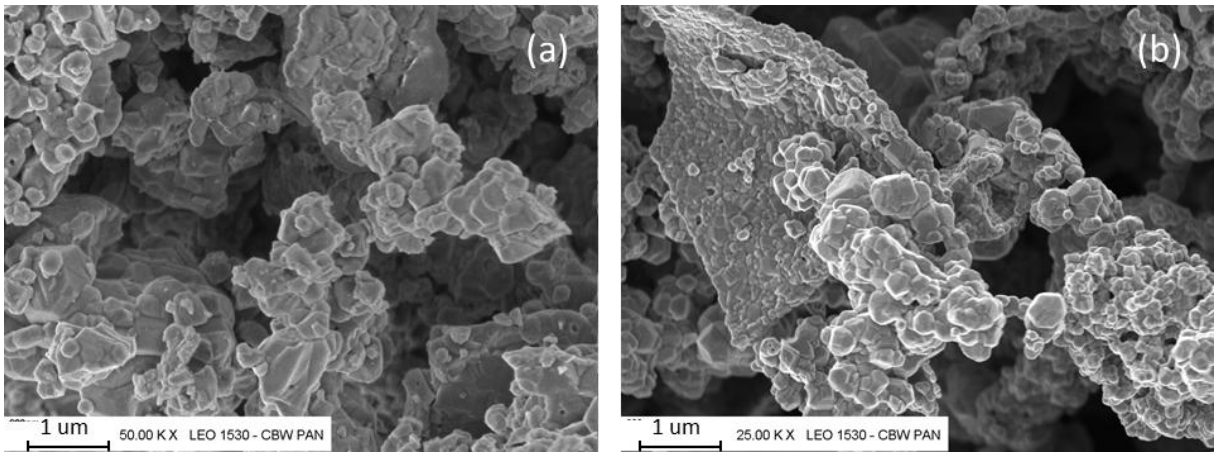

Fig. 2. SEM images of (a) C-$LiMn_2O_4$ and (b) E-$LiMn_2O_4$ samples.

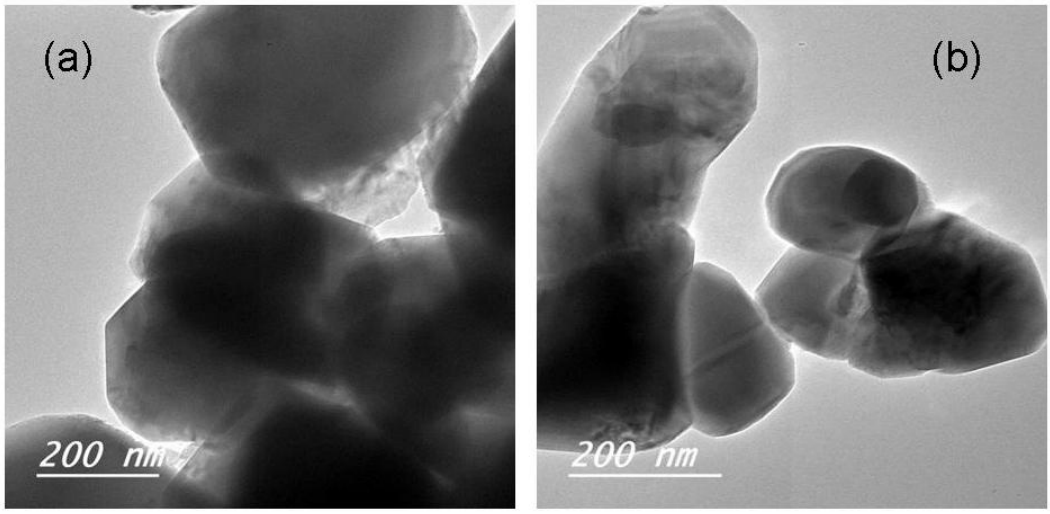

Fig. 3. TEM images of (a) C-$LiMn_2O_4$ and (b) E-$LiMn_2O_4$ samples.

3.2. Spectroscopic properties

Among the local probes, Raman scattering (RS) and Fourier transform infrared (FTIR) spectroscopy are techniques sensitive to the short-range environment of oxygen coordination around the cations [34]. As a first approximation, the spectra consist of a superposition of the components of all local entities present in the same material in contrast to diffraction data, which give a weighted average. As a rule, the frequency and relative intensity of the bands are sensitive to coordination geometry and oxidation states [35]. In $LiMn_2O_4$, the Li, Mn and O occupy 8*a*, 16*d* and 32*e* (Wyckoff position) sites, respectively. The vibration modes associated to each

transition metal-ion are decomposed as $\Gamma = A_{1g}(R) + E_g(R) + 3T_{2g}(R) + 4T_{iu}(ir) + T_{1g} + 2A_{2u} + 2E_u + 2T_{2u}$, where (R) and (ir) denote Raman and infrared active modes, respectively, and the remaining modes are silent [36, 37].

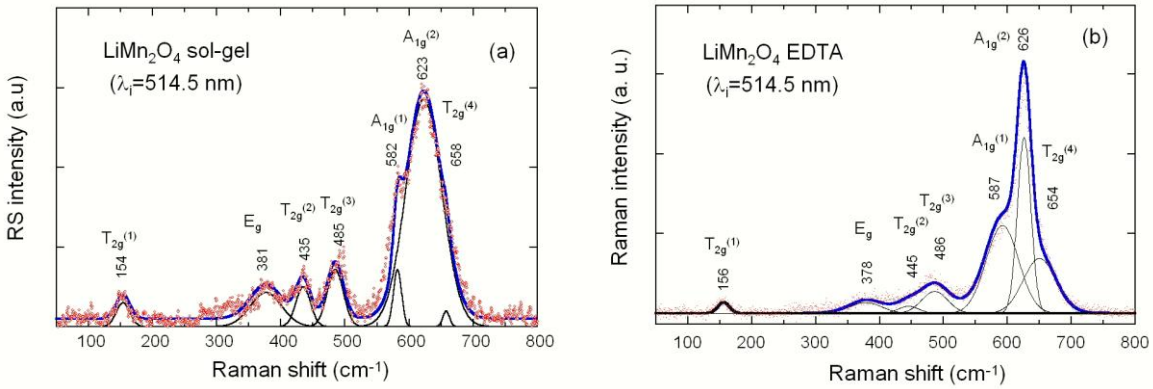

Fig. 4. Raman spectra for $LiMn_2O_4$ powders with chelating agent (a) citric acid and (b) EDTA prepared by sol-gel method.

Figures 4(a-b) shows the Raman spectra of C- and E-$LiMn_2O_4$ spinel in the spectral region of 100-800 cm^{-1}, which is divided into two groups of bands (i) weak bands in the range 200-500 cm^{-1} and (ii) strong bands around 600 cm^{-1}, in agreement with prior works [38]. The RS spectrum of $LiMn_2O_4$ is dominated by a band at 623-626 cm^{-1}. This is the symmetric A_{1g} Mn–O stretching vibration of MnO_6 octahedral units. The A_{1g} broadening in two samples is related with the polyhedral distortion occurring in $LiMn_2O_4$ resulting in the observation of the stretching vibrations of MnO_6^{9-} and MnO_6^{8-} octahedra [35,36]. The smaller broadening of the A_{1g} band in the E-$LiMn_2O_4$ is thus an evidence of the smaller strain field in this sample, in agreement with the data in Table 1. The shoulder at 587 and 583 cm^{-1} respectively of the $T^{(1)}_{2g}$ mode in this region is not well separated because of its low intensity. In the localized-vibration approach it is speculated that the intensity of the Raman shoulder is closely related to the manganese average oxidation state in the spinel phase. Because the intensity of this shoulder is very sensitive to the lithium stoichiometry, it is suggested that its character originates mainly from the vibration of Mn^{4+}–O bonding. The RS peak with medium intensity located at 486cm^{-1} has $T^{(2)}_{2g}$ symmetry where the two weak bands observed at 445, 378 cm^{-1} and 435, 386 cm^{-1} for C- and E-$LiMn_2O_4$ samples, respectively, have the E_g and $T^{(3)}_{2g}$ symmetry. The $T^{(3)}_{2g}$ mode is related to the Li–O

motion, i.e. connected to the tetrahedral cation movements. A broad and very weak band at 156±2 cm^{-1} is attributed to the translation mode of lattice vibration, i.e. T_{2g}(T) mode.

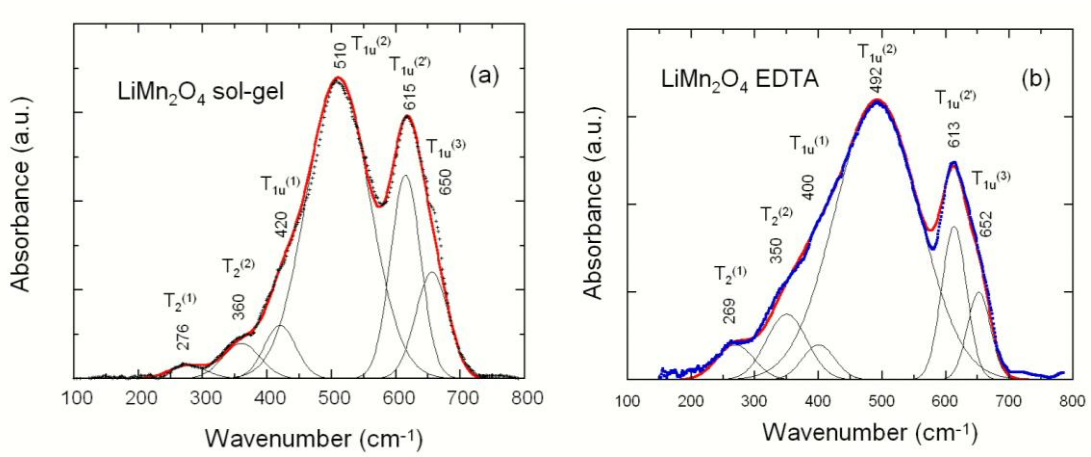

Fig. 5. FTIR spectra of (a) C-$LiMn_2O_4$ and (b) E-$LiMn_2O_4$ prepared by sol-gel method using chelating agent citric acid and EDTA, respectively.

The FTIR spectra in Figs. 5(a,b) are dominated by two intense high-frequency absorption bands at approximately 615, 613 cm^{-1} and 510, 492 cm^{-1}, respectively, and they are attributed to the asymmetric stretching modes of the MnO_6 group. All the IR bands belong to the (F_{1u}) species. Three weak bands are observed in the low-frequency region at approximately 420, 360, 276 cm^{-1} and 400, 350, 269 cm^{-1}, respectively, and have a mixed character due to the presence of the bending modes of O-Mn-O bonds and modes of LiO_4 groups [34-38]. The RS and FTIR spectra of the E-$LiMn_2O_4$ and C-$LiMn_2O_4$ are the same but a small shift in peaks of EDTA is observed due to decrease in the lattice parameters. Especially the cell volume and the broadening of the peaks are observed due to local distortion of the lattice associated to the Jahn-Teller Mn^{3+} ion. The presence of this ion also breaks the translational invariance and is responsible for the larger number of vibration modes revealed by the decomposition of the spectra illustrated in Figs 4 and 5.

The ^{7}Li MAS NMR spectra of the two $LiMn_2O_4$ samples are shown in Fig. 6. They are dominated by a strong peak at 524 ppm. This peak belongs to the Li ions located on the tetrahedral (8*a*) sites of the spinel structure. The large shift is caused by the unpaired electron spin density that is transferred from the Mn ions via Mn-O-Li bonds to the Li nuclei [39-41]. Fast electron hopping between the Mn ions results in an average oxidation state of the Mn ions

of +3.5, as seen by NMR spectroscopy. Additional peaks are observed at 655 ppm, 601 ppm, and 564 ppm. These are caused by an increased number of Mn^{4+} ions (with an average Mn oxidation state +3.56), as they occur in excess-Li spinels ($Li_{1.05}Mn_{1.95}O_4$) [40], which is also the actual composition of the C-LMO, while the E-LMO is stoichiometric, in agreement with XPS results. The amount of Mn^{4+} is higher in the C-$LiMn_2O_4$ sample in comparison with the E-$LiMn_2O_4$ sample, which illustrates that the NMR measurements are actually more sensitive than XRD, since the error in the determination of the lattice parameter of C-$LiMn_2O_4$ did not allow us to determine the Mn^{4+}/Mn^{3+} ratio in this sample.

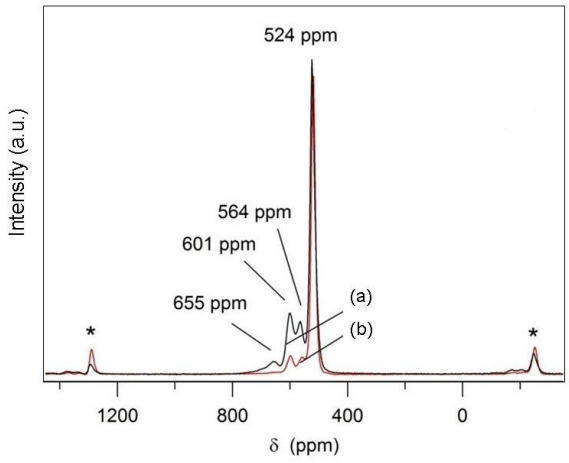

Fig. 6. ^{7}Li MAS NMR spectra of the two $LiMn_2O_4$ samples (a) C-$LiMn_2O_4$ and (b) E-$LiMn_2O_4$. Spinning sidebands are marked with an asterisk.

X-ray photoelectron spectroscopy (XPS) was employed in evaluating the chemical state of Mn cations. Figure 7 displays the XPS spectra of Mn $2p_{3/2}$ and Mn$2p_{1/2}$ core levels for (a) C-$LiMn_2O_4$ and (b) E-$LiMn_2O_4$ samples. Deconvolution was performed with the binding energy positions of Mn^{3+} and Mn^{4+} ions taken at 642.1 and 643.6 eV, respectively. These binding energies correspond to that of $Mn^{III}{}_2O_3$ and of $Mn^{IV}O_2$ as reported by Ramana et al. [42] and Shin et al. [43]. The analysis shows that the valence state of Mn in C-$LiMn_2O_4$ is 3.56 against 3.505 in E-$LiMn_2O_4$. These results confirm the modification of the cubic lattice parameters observed by XRD and are in good agreement with the NMR measurements.

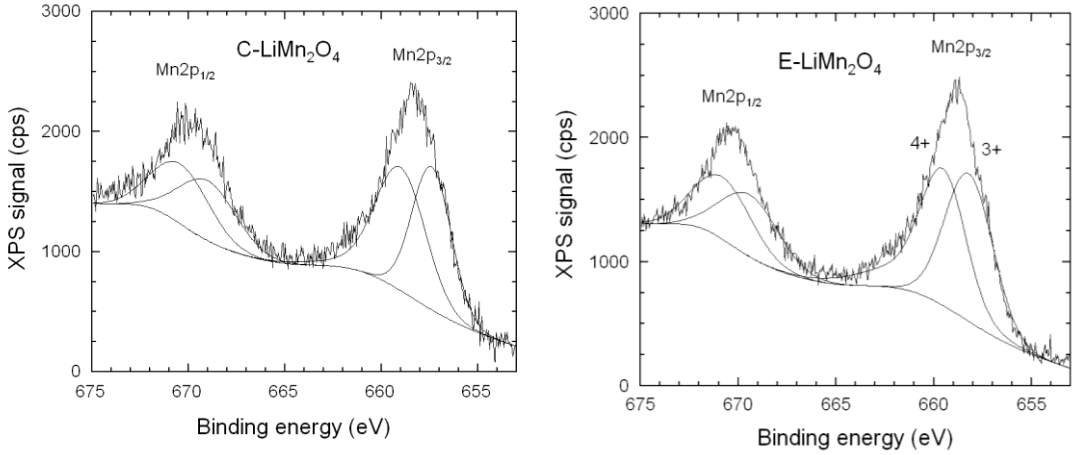

Fig. 7. XPS spectra of Mn $2p_{3/2}$ and Mn$2p_{1/2}$ core levels for C-$LiMn_2O_4$ and E-$LiMn_2O_4$ samples. Deconvolution was performed with the binding energy positions of Mn^{3+} and Mn^{4+} ions taken at 642.1 and 643.6 eV, respectively.

3.3. Electrochemical properties

The first five cyclic voltammograms of E-$LiMn_2O_4$ and C-$LiMn_2O_4$ at a scan rate of 0.05 mVs^{-1} in the voltage range 3.5-4.5 V vs. Li^+/Li^0 are shown in Figs. 8 and 9, respectively. Similar but not identical CV curves were observed with two redox peaks located at 4.10/4.05 V and 4.22/3.92 V in Fig. 8a for E-$LiMn_2O_4$ and 4.22/4.05 V and 4.12/3.91 V in Fig. 8b for C-$LiMn_2O_4$. The anodic and cathodic peaks are related, respectively to the extraction and insertion of Li^+ in the tetrahedral sites of the structural matrix of the spinel. The two prepared samples showed almost the same difference between anodic and cathodic potential (potential interval ΔE between the oxidation and reduction) indicating good reversibility in the cycling process during lithium intercalation/de-intercalation. Furthermore, in Fig. 8a the observed peaks are relatively sharper than the peaks observed in Fig. 8b, another evidence of the higher crystallinity of the E-$LiMn_2O_4$ electrode in comparison to that of C-$LiMn_2O_4$.

Galvanostatic charge-discharge curves of E-$LiMn_2O_4$ and C-$LiMn_2O_4$ samples at 0.1C rate (1C = 148 mAh g^{-1}) in the voltage range 3.0-4.5 V vs. Li^+/Li^0 are shown in Figs. 9a and 9b, respectively. Two consecutive slowly increasing (for charge) or decreasing (for discharge) plateaus, one at 3.97/4.12 V and the other at 4.11/3.97 V are observed for E-$LiMn_2O_4$ (Fig. 7a). In Fig. 9b, the two plateaus for charge and discharge of C-$LiMn_2O_4$ are observed at 3.97/4.12 V and 4.18/4.0 V, respectively. These voltage plateaus are commonly observed for $LiMn_2O_4$-based

electrodes. They are attributed to the two-step cubic phase transformations of $LiMn_2O_4/Li_{0.5}Mn_2O_4$ and $Li_{0.5}Mn_2O_4/\lambda$-MnO_2 during oxidation and the reverse during reduction [44].

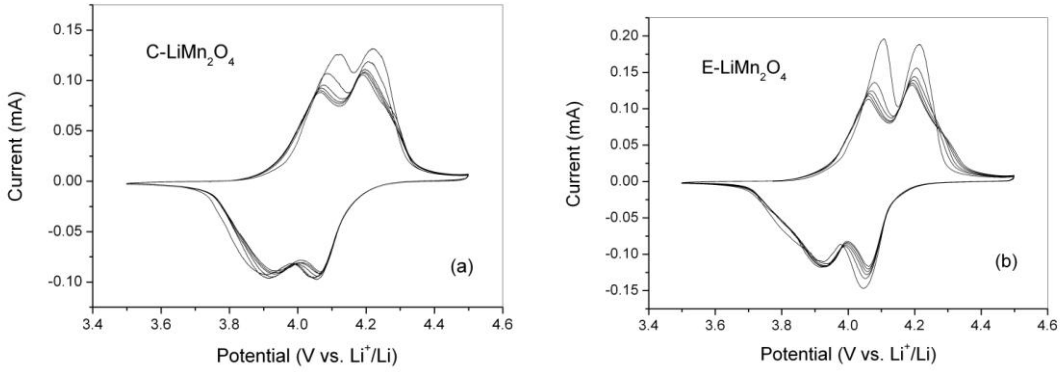

Fig. 8. Cyclic voltammograms recorded at a scan rate of 0.05 mV s^{-1} in the voltage range 3.5-4.5 V vs. Li^+/Li^0 for (a) C-$LiMn_2O_4$ and (b) E-$LiMn_2O_4$.

As shown in Fig. 9, the initial charge and discharge specific capacities of the prepared E-$LiMn_2O_4$ sample are 132 and 123 mAh g^{-1}, respectively, with a coulombic efficiency of 93.6%. About 84 % of the theoretical capacity (Q_{th}=148 mAh g^{-1}) was obtained for discharging E-$LiMn_2O_4$ electrode corresponding to the re-lithiation degree of $Li_{0.84}Mn_2O_4$. Therefore, most parts of the electrode materials were electrochemically active for the lithium insertion reaction. C-$LiMn_2O_4$ was discharged to $Li_{0.82}Mn_2O_4$, which means 82% of the theoretical capacity was obtained and the sample has 91.7 % coulombic efficiency in the first cycle as shown in Fig.9b.

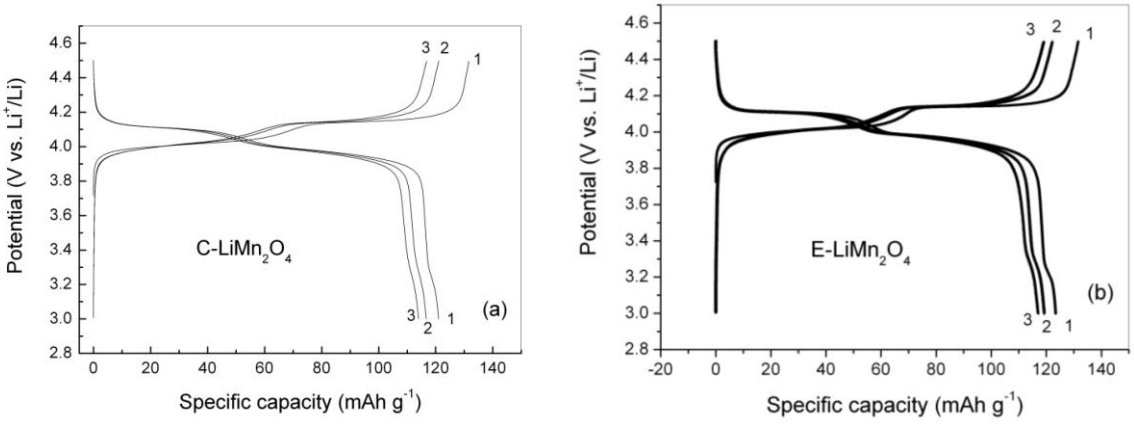

Fig. 9. Charge–discharge curves of (a) C-$LiMn_2O_4$ and (b) E-$LiMn_2O_4$ electrode taken at 0.1C between 3.0 and 4.5 V vs. Li^+/Li^0.

Figure 10a illustrates the cycle performance of the prepared samples between 3.0 – 4.5 V vs. Li^+/Li^0 at various C-rate. The cycleability of the LMO samples recorded at 0.5C rate over 35 cycles is shown in Fig. 10b. After 35 cycles in the 4 V region, the discharge capacity of the prepared E-$LiMn_2O_4$ and C-$LiMn_2O_4$ reduced to 96 and 85 mAh g^{-1}, respectively, corresponding to 78% and 70% of the initial capacity. It is obvious that capacity fades for the two prepared samples is more significant in the first 10 cycles, probably due to the cell formation, dissolution of cathode material and side reactions [6,45]. The coulombic efficient is also reported in Fig. 10b. Indeed, the surface area of the SEI is increased when the particles are smaller, which will result in a smaller coulombic efficiency in the first cycle during the formation of the SEI. However, for the subsequent cycles, this is the opposite: the coulombic efficiency is increased because it is easier to extract all the lithium from a small particle than from a big particle.

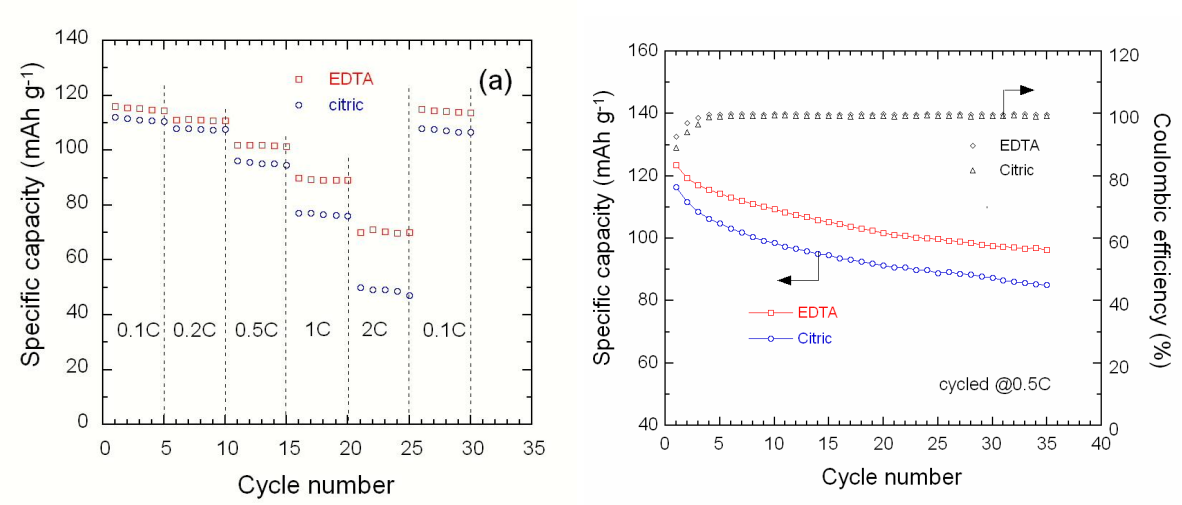

Fig. 10. Cyclic performance of C-$LiMn_2O_4$ and E-$LiMn_2O_4$ samples: (a) Specific discharge capacity at various C-rates. (b) Specific discharge capacity vs. cycle number at rate.

3.4. Discussion

According to our results, despite the beneficial effect of EDTA on the structural properties of $LiMn_2O_4$, the impact on the electrochemical properties is marginal. One reason is that this chelating agent did not modify the size of the particles, while better results would be expected with nanostructured particles [4,46-48]. Another reason is that the choice of EDTA fails to stabilize the spinel structure. For this purpose, different methods can be used. Doping, particularly by substituting oxygen with sulfur stabilizes the spinel structure by reducing the

octahedral symmetry [49-50]. The capacity fading comes from the Jahn-Teller distortion associated with the Mn^{3+} ions. The reduction of such distortions can be obtained by substitution of Mn^{3+} by another trivalent ion. We have already mentioned Y^{3+} and Nd^{3+} [32,33]; Ni^{3+} substitution for Mn^{3+} also stabilizes the spinel structure [51]. Synergetic effects combining sulfur and nickel doping have been obtained [52-54]. To overcome the problem of the dilution of the manganese into the electrolyte when $LiMn_2O_4$ is delithiated, a surface modification is efficient [55-60]. A combination of these strategies can be done to improve both the energy density and cycle life [61].

The electrochemical properties of any cathode material do not only depend on the choice of the chelating agent. It is well known that they also depend importantly on the morphology (size and shape) of the particles, and on the synthesis temperature. These parameters are not independent. Therefore, it is not possible to change the chelating agent and fix both the morphology and the synthesis temperature at the same time. Considering the products with similar particle size, it has been currently demonstrated that $LiMn_2O_4$ with good crystallinity must be prepared at T>600 °C. For example, Jin et al. [1] obtained well-shaped octahedral LMO grains by a two-step synthesis at 700 °C; Zhao et al. [3] prepared LMO at 750 °C using a sol-gel method assisted by citric acid; calcination at 600 °C for 5h achieved nanocrystalline LMO (≈80 nm) prepared by combustion method [4]; LMO nanoparticles (165 nm average size) were obtained by precipitation method and sintering at 800 °C for 10 h [50]; nanocrystalline LMO particles were prepared by an ultrasonic spray pyrolysis method using nitrate salts at 800 °C in air atmosphere [5]; the solid-state combustion method requested a calcination at 800 °C for 10 h to obtain grain size ≈100 nm; well-crystallized LMO synthesized by cellulose-citric acid method was sintered at 750-900 °C for 10 h [46]; a combustion method using urea as a fuel was developed to grow LMO at T≈500 °C [62]; submicronic LMO powders were prepared using a methanolic solution of metal acetates and succinic acid with sintering at 800 °C [63]; microwave-heated LMO powders were prepared at 800 °C by Fu et al. [15]; homogeneous particles (≈300-400 nm sized) were prepared by micro-emulsion method with sintering at 800 °C [12]; 300-nm LMO nanoparticles were grown by hydrothermal synthesis following by sintering at 700 °C for 10 h [46]; LMO submicron-crystal LMO were prepared by ball milling and heat treated in the range 750-900 °C [30]; Molenda et al. [50] reported the growth of nanosized LMO

using a modified sol-gel method followed by calcination at 650 °C. To conclude, there is an experimental fact that 650 °C is the lowest temperature to prepare nanocrystalline LMO.

Here, we have chosen to fix the morphology, and thus adjust the synthesis temperature of the C-$LiMn_2O_4$ to reproduce the same shape and size as the E-$LiMn_2O_4$ prepared at 650 °C. We had to rise the temperature to 800 °C for the C-$LiMn_2O_4$ for this purpose. The other approach would be to fix the synthesis temperature to 650 °C, but in that case, the morphology will change if the same synthesis process is kept. However, it is possible to find a synthesis process that gives a material synthesized at the same temperature 650 °C and morphology comparable to that of the E-$LiMn_2O_4$ sample. This mode of preparation is the rheological-phase-assisted microwave synthesis method [64]. Using this method, Cui et al. have investigated the effect of the temperature in the range 600 – 900 °C, which is the typical range used to synthesize the spinel by different processes. As a result, they found that this synthesis is superior in terms of regular shapes with respect to other synthesis methods including solid-state reaction sol–gel synthesis, precipitation, and Pechini process. Although the particles have a more cubic shape than in the E-$LiMn_2O_4$ sample, the size of the particles is comparable for a synthesis temperature. However, in this case the initial capacity is 100 mAh g^{-1}, and more importantly reduces to circa 45 mAh g^{-1} after 25 cycles. The measurements in [64] have been made at rate C/3 rate. The rate capability of the E-$LiMn_2O_4$, reported in Fig. 8b up to 0.5C rate, shows the superiority of the E-$LiMn_2O_4$ with respect to the results in [64], which illustrates the efficiency of the sol-gel synthesis with the chelating agent chosen in the present work.

4. Conclusion

Single phase cubic spinel $LiMn_2O_4$ phase with a space group *Fd*3*m* was obtained in this study by using EDTA and citric acid as chelating agents. Well-crystallized spinel powders were obtained after calcination at 650 °C by using EDTA as chelating agent, while a sintering at 800 °C was performed to get the same morphology and size of $LiMn_2O_4$ particles prepared via citric acid. This reduction in preparation temperature makes this technique cost-effective. Due to its molecular configuration of EDTA, i.e. four carboxylic and two amine functions, its role as a hexadentate chelating agent provide material with better structural properties. Even if the use of EDTA as chelating agent improves the structural stability and increases slightly the capacity, the results in the present work show that the surface modifications and doping of nanostructured

$LiMn_2O_4$ are mandatory to obtain a cathode that is competitive for commercial use. Among the wet-chemical methods, the EDTA-assisted synthesis saves both reaction time and energy. It also gives superior electrochemical properties with respect to particles of the same size and shape prepared by other techniques or with respect to $LiMn_2O_4$ particles synthesized at the same temperature.

Acknowledgement

Some part of this work has benefited from financial support within the BMBF project "DESIREE", grant number 03SF0477B.

References

[1] G. Jin, H. Wang, H. Xie, H. Wang, K. He, P. Liu, J. Chen, Y. Tang, S. Liu, C. Huang, Synthesis of single-crystalline octahedral $LiMn_2O_4$ as high performance cathode for Li-ion battery. Electrochim. Acta 150 (2014) 1-7.

[2] M. S. Whittingham, Lithium batteries and cathode materials. Chem. Rev. 104 (2004) 4271-4301.

[3] H. Zhao, F. Li, X. Liu, C. Cheng, Z. Zhang, Y. Wu, W. Xiong, B. Chen, Effects of equimolar Mg (II) and Si (IV) co-doping on the electrochemical properties of spinel $LiMn_{2-2x}Mg_xSi_xO_4$ prepared by citric acid assisted sol–gel method. Electrochim. Acta 151 (2015) 263-269.

[4] X. Gao, Y. Sha, Q. Lin, R. Cai, O.M. Tade, Z. Shao, Combustion-derived nanocrystalline $LiMn_2O_4$ as a promising cathode material for lithium-ion batteries. J. Power Sources 275 (2015) 38-44.

[5] B. Ebin, V. Battaglia, S. Gürmen, Comparison of 4 V and 3 V electrochemical properties of nanocrystalline $LiMn_2O_4$ cathode particles in lithium ion batteries prepared by ultrasonic spray pyrolysis. Ceram. Int. 40 (2014) 7029-7035.

[6] D. K. Kim, P. Muralidharan, H. W. Lee, R. Ruffo, Y. Yang, C. K. Chan, H. L. Peng, R. A. Huggins, Y. Cui, Spinel $LiMn_2O_4$ nanorods as lithium ion battery cathodes. Nano Lett. 8 (2008) 3948-3952.

[7] Y. Cai, Y. Huang, X. Wang, D. Jia, X. Tang, Long cycle life, high rate capability of truncated octahedral $LiMn_2O_4$ cathode materials synthesized by a solid-state combustion reaction for lithium ion batteries. Ceram. Int. 40 (2014)14039-14043.

[8] C. M. Julien, A. Mauger, A. Vijh, K. Zaghib, Lithium Batteries: Science and Technology, Springer, Cham, 2016.

[9] Y. G. Guo, J. S. Hu, L. J. Wan, Nanostructured Materials for Electrochemical Energy Conversion and Storage devices. Adv. Mater. 20 (2008) 2878-2887.

[10] Y. Wang, G. Cao, Developments in nanostructured cathode materials for high-performance lithium-ion batteries. Adv. Mater. 20 (2008) 2251-2269.

[11] M. E. Lines, A. M. Glass, Principles and applications of ferroelectrics and related materials, Clarendon: Oxford, U.K., 1977.

[12] D. Ke, H. G. Rong, P. Z. Dong, Q. Lu, Synthesis of spinel $LiMn_2O_4$ with manganese carbonate prepared by micro-emulsion method. Electrochim. Acta 55 (2010) 1733-1739.

[13] T. Tsuji, M. Nagao, Y. Yamamura, N. T. Tai, Structural and thermal properties of $LiMn_2O_4$ substituted for manganese by iron. Solid State Ionics 154–155 (2002) 381-386.

[14] M. Michalska, L. Lipinska, M. Mirkowska, M. Aksienionek, R. Diduszko, M Wasiucionek, Nanocrystalline lithium-manganese oxide spinels for Li-ion batteries: sol-gel synthesis and characterization of their structure and selected physical properties. Solid State Ionics 188 (2011) 160-164.

[15] Y.-P. Fu, Y.-H. Su, C.-H. Lin, S.-H. Wu, Comparison of the microwave-induced combustion and solid state reaction for the synthesis of $LiMn_2O_4$ powder and their electrochemical properties. Ceram. Int. 35 (2009) 3463-3468.

[16] C. Wan, M. Wu, D. Wu, Synthesis of spherical $LiMn_2O_4$ cathode material by dynamic sintering of spray-dried precursors. Powder Technol. 199 (2010) 154-158.

[17] X. Zhang, A.-G. Porras-Gutierrez, A. Mauger, H. Groult, C. M. Julien, Nanotechnology of positive electrodes for Li-ion batteries. Inorganics 5 (2017) 25.

[18] J. Liu, Z. Wen, Z. Gu, M. Wu, Z. Lin, Synthesis by an EDTA-based soft-chemistry route and characterization of nanosized $LiCoO_2$ cathode materials. J. Electrochem. Soc. 149 (2002) A1405-A1408.

[19] L. Han, J. Zhu, L. Wang, Y. Gao, Preparation of lithium battery cathode materials $Li_{1-x}K_xCoO_2$ by EDTA complexing method. Rare Metal Mater. Eng. 36 (2007) 627-630.

[20] K.A. Jarvis, Z. Deng, L. F. Allard, A. Manthiram, P. J. Ferreira, Understanding structural defects in lithium-rich layered oxide cathodes. J. Mater. Chem. 22 (2012) 11550-11555.

[21] Z. Yuan, H. Yue, X. Zhang, X. Deng, Preparation and characterization of LiV_3O_8 cathode material for lithium secondary batteries through an EDTA sol-gel method. Solid State Ionics 179 (2008) 1763-1767.

[22] P. Dong, S.-B. Xia, Y.-J. Zhang, Y.-N. Zhang, Z.-P. Qiu, Y. Yao, Influence of complexing agent on the structure and electrochemical properties of $LiNi_{0.80}Co_{0.15}Al_{0.05}O_2$ cathode synthesized by sol-gel method: a comparative study. Int. J. Electrochem. Sci. 12 (2017) 561-575.

[23] Y. Li, L. Hong, J. Sun, F. Wu, S. Chen, Electrochemical performance of $Li_3V_2(PO_4)_3$/C prepared with a novel carbon source, EDTA. Electrochim. Acta 85 (2012) 110-115.

[24] W.-H. Yuan, C.-Y. Wang, L. Li, Preparation and property of normal spinel $LiMn_2O_4$. J. South China University of Technology (Natural Science) 35 (2007) 81-85.

[25] M.-J. Lee, S. Lee, P. Oh, Y. Kim, J. Cho, High performance $LiMn_2O_4$ cathode materials grown with epitaxial layered nanostructure for Li-ion batteries. Nano Lett. 14 (2014) 993-999.

[26] L. Duan, X. Zhang, K. Yue, J. Zhuang, W. Lu, Synthesis and electrochemical property of LiMn2O4 porous hollow nanofiber as cathode for lithium-ion batteries. Nanoscale Res. Lett. 12 (2017) 109.

[27] P. Ram, A. Gören, S. Ferdov, M. M. Silva, R. Singhal, C. M. Costa, R. K. Sharma, S. Lanceros-Mendez, Improved performance of rare earth doped LiMn2O4 cathodes for lithium-ion battery applications. New J. Chem. 40 (2016) 6244.

[28] B. S Liu, Z. B Wang, Y. Zhang, F. D. Yu, Y. Xue, K. Ke, F.-F. Li, Preparation of sub microcrystal $LiMn_2O_4$ used Mn_3O_4 as precursor and its electrochemical performance for lithium ion battery. J. Alloys Compds 622 (2015) 902-907.

[29] G. Yuan, J. Bai, T.N.L. Doan, P. Chen, Synthesis and electrochemical investigation of nano-sized $LiMn_2O_4$ as cathode material for rechargeable hybrid aqueous batteries. Mater. Lett. 137 (2014) 311-314.

[30] Y.B.R.D. Rajesh, R. S. Dubey, Sol-gel synthesis and characterization of nano crystalline spinel $LiMn_2O_4$ for battery application. NanoSci. NanoEng. 1 (2013)139-141.

[31] T.-F. Yia, C.-L. Haob, C.-B. Yuea, R.-S. Zhua, J. Shu, A literature review and test: Structure and physicochemical properties of spinel $LiMn_2O_4$ synthesized by different temperatures for lithium ion battery. Synthetic Metals 159 (2009) 1255-1260.

[32] C. Feng, H. Tang, K. Zhang, J. Sun, Synthesis and electrochemical characterization of nonstoichiometry spinel phase ($Li_xMn_{1.93}Y_{0.02}O_4$) for lithium ion battery applications. Mater. Chem. Phys. 80 (2003) 573-576.

[33] S. Balaji, T. Manichandran, D. Mutharasu, A comprehensive study on influence of Nd^{3+} substitution on properties of $LiMn_2O_4$. Bull. Mater. Sci. 35 (2012) 471-480.

[34] C.M. Julien, M. Massot, Lattice vibrations of materials for lithium rechargeable batteries III. Lithium manganese oxides. Mater. Sci. Eng. B 100 (2003) 69-78.

[35] C.M. Julien, M. Massot, Lattice vibrations of materials for lithium rechargeable batteries I. Lithium manganese oxides. Mater. Sci. Eng. B 97 (2003) 217-230.

[36] C.M. Julien, F. Gendron, A. Amdouni, M. Massot, Lattice vibrations of materials for lithium rechargeable batteries. VI: Ordered spinel. Mater. Sci. Eng. B 130 (2006) 41-48.

[37] C.M. Julien, M.A. Camacho-Lopez, Lattice vibrations of materials for lithium rechargeable batteries II. Lithium extraction–insertion in spinel structures. Mater. Sci. Eng. B 108 (2004) 179-186.

[38] C.M. Julien, M. Massot, S. Rangan, M. Lemal, D. Guyomard, Study of structural defects in γ-MnO_2 by Raman spectroscopy. J. Raman Spectrosc. 33 (2002) 223-228.

[39] Y.J. Lee, F. Wang, C.P. Grey, ^{6}Li and ^{7}Li MAS NMR studies of lithium manganate cathode materials. J. Am. Chem. Soc.120 (1998) 12601-12613.

[40] Y.J. Lee, C.P. Grey, ^{6}Li magic angle spinning nuclear magnetic resonance study of the cathode materials $Li_{1+\alpha}Mn_{2-\alpha}O_{4-\delta}$. The effect of local structure on the electrochemical properties. J. Electrochem. Soc. 149 (2002) A103-A114.

[41] C.P. Grey, N. Dupré, NMR studies of cathode materials for lithium-ion rechargeable batteries. Chem. Rev. 104 (2004) 4493-4512.

[42] C.V. Ramana, M. Massot, C.M. Julien, XPS and Raman spectroscopic characterization of $LiMn_2O_4$ spinels. Surf. Interface Anal. 37 (2005) 412-416.

[43] D.W. Shin, J.W. Choi, W.K. Choi, Y.S. Cho, S.J. Yoon, XPS/EXAFS study of cycleability improved $LiMn_2O_4$ thin films cathodes prepared by solution deposition. Electrochem. Commun. 11 (2009) 695-698.

[44] D. Tonti, M. J. Torralvo, E. Enciso, I. Sobrados, J. Sanz, Three-dimensionally ordered macroporous lithium manganese oxide for rechargeable lithium batteries. Chem. Mater. 20 (2008) 4783-4790.

[45] M. Wakihara, H. Ikuta, Y. Uchimoto, Structural stability in partially substituted lithium manganese spinel oxide cathode. Ionics 8 (2002) 329-338.

[46] H.B. Lin, J.N. Hu, H.B. Rong, Y.M. Zhang, S.W Mai, L.D. Xing, M.Q. Xu, X.P. Li, W.S. Li, Porous $LiMn_2O_4$ cubes architecture with single-crystalline nanoparticles and exhibiting excellent cyclic stability and rate capability as the cathode of a lithium ion battery. J. Mater. Chem. A 2 (2014) 9272-9279.

[47] Y. Cai, Y. Huang, X. Wang, D. Jia, W. Pang, Z. Guo, Y. Du, X. Tang, Facile synthesis of $LiMn_2O_4$ octahedral nanoparticles as cathode materials for high capacity lithium ion batteries with long cycle life. J. Power Sources 278 (2015) 574-581.

[48] H. Zhao F. Li, X. Liu, W. Xiong, B. Chen, H. Shao, D. Que, Z. Zhang, Y. Wu, A simple, low-cost and eco-friendly approach to synthesize single-crystalline $LiMn_2O_4$ nanorods with high electrochemical performance for lithium-ion batteries. Electrochim. Acta 166 (2015) 124-133.

[49] Q. Jiang, D. Liu, H. Zhang, S. Wang, Plasma-assisted sulfur doping of $LiMn_2O_4$ for high-performance lithium-ion batteries. J. Phys. Chem. C 119 (2015) 28776-28782.

[50] M. Molenda, M. Bakierska, D. Majda, M. Swietosławski, R. Dziembaj, Structural and electrochemical characterization of sulphur-doped lithium manganese spinel cathode materials for lithium ion batteries. Solid State Ionics 272 (2015) 127-132.

[51] L. Hernán, J. Morales, L. Sánchez, E. Rodríguez-Castellón, E. M.A.G. Aranda, Synthesis, characterization and comparative study of the electrochemical properties of doped lithium manganese spinels as cathodes for high voltage lithium batteries. J. Mater. Chem. 12 (2002) 734-741.

[52] Y. K. Sun, S. W. Oh, C. S. Yoon, H. J. Bang, J. Prakash, Effect of sulfur and nickel doping on morphology and electrochemical performance of $LiNi_{0.5}Mn_{1.5}O_{4-x}S_x$ spinel material in 3-V region. J. Power Sources 161 (2006) 19-26.

[53] M. W. Raja, S. Mahanty, R. N. Basu, Influence of S and Ni co-doping on structure, band gap and electrochemical properties of lithium manganese oxide synthesized by soft chemical method. J. Power Sources 192 (2009) 618-626.

[54] M. Bakierska, M. Swietosławski, M. Gajewska, A. Kowalczyk, Z. Piwowarska, L. Chmielarz, R. Dziembaj, M. Molenda, Enhancement of electrochemical performance of $LiMn_2O_4$ spinel cathode material by synergetic substitution with Ni and S. Materials 9 (2016) 366.

[55] J. Wang, Q. Zhang, X. Li, Z. Wang, H. Guo, D. Xu, K. Zhang, Sputtering graphite coating to improve the elevated-temperature cycling ability of the $LiMn_2O_4$ electrode. Phys. Chem. Chem. Phys. 16 (2014) 16021-16029.

[56] J. Zeng, M. Li, X. Li, C. Chen, D. Xiong, L. Dong, D. Li, A. Lushington, X. Sun, A novel coating onto $LiMn_2O_4$ cathode with increased lithium ion battery. Appl. Surf. Sci. 317 (2014) 884-891.

[57] J. Wang, S. Yao, W. Lin, B. Wu, X. He, J. Li, J. Zhao, Improving the electrochemical properties of high-voltage lithium nickel manganese oxide by surface coating with vanadium oxides for lithium ion batteries. J. Power Sources 280 (2015) 114-124.

[58] R. Jiang, C. Cui, H. Ma, H. Ma, T. Chen, Study on the enhanced electrochemical performance of $LiMn_2O_4$ cathode material at 55 °C by the nano Ag-coating. J. Electroanal. Chem. 744 (2015) 69-76.

[59] T. Wang, W. Wang, D. Zhu, L. Huang, Y. Chen, Improvement of the overall performances of $LiMn_2O_4$ via surface-modification by polypyrrole. Mater. Res. Bull. 71 (2015) 91-97.

[60] Y. Shang, X. Lin, X. Lu, T. Huang, A. Yu, Nano-TiO_2(B) coated $LiMn_2O_4$ as cathode materials for lithium-ion batteries at elevated temperatures. Electrochim. Acta 156 (2015) 121-126.

[61] M. Molenda, R. Dziembaj, E. Podstawka, L. M. Proniewicz, Z. Piwowarska, An attempt to improve electrical conductivity of the pyrolyzed carbon-$LiMn_2O_{4-y}S_y$ ($0 \leq y \leq 0.5$) composites. J. Power Sources 174 (2007) 613-618.

[62] S. Chitra, P. Kalyani, T. Mohan, M. Massot, S. Ziolkiewicz, R. Gangandharan, M. Eddrief, C. Julien, Physical properties of $LiMn_2O_4$ spinel prepared at moderate temperature. Ionics 4 (1998) 8–15.

[63] S.R.S. Prabaharan, S.S. Michael, C. Julien, Synthesis and electrochemistry of $LiMn_2O_4$ prepared using succinic acid as complexing agent. Int. J. Inorg. Mater. 1 (1999) 21-27.

[64] T. Cui, N. Hua, Y. Han, K. Kang, Synthesis and electrochemical property of $LiMn_2O_4$ porous hollow nanofiber as cathode for lithium-ion batteries. Inorg. Mater. 44 (2008) 542-548.

Figure Captions

Fig. 1. (a) X-ray diffraction patterns of C-$LiMn_2O_4$ and E-$LiMn_2O_4$. (b) Analysis of the fullwidth at half-maximum B of the Bragg reflections.

Fig. 2. SEM images of (a) C-$LiMn_2O_4$ and (b) E-$LiMn_2O_4$ samples.

Fig. 3. TEM images of (a) C-$LiMn_2O_4$ and (b) E-$LiMn_2O_4$ samples.

Fig. 4. Raman spectra for $LiMn_2O_4$ powders with chelating agent (a) citric acid and (b) EDTA prepared by sol-gel method.

Fig. 5. FTIR spectra of (a) C-$LiMn_2O_4$ and (b) E-$LiMn_2O_4$ prepared by sol-gel method using chelating agent citric acid and EDTA, respectively.

Fig. 6. ^{7}Li MAS NMR spectra of the two $LiMn_2O_4$ samples (1) C-$LiMn_2O_4$ and (2) E-$LiMn_2O_4$. Spinning sidebands are marked with an asterisk.

Fig. 7. XPS spectra of Mn $2p_{3/2}$ and Mn$2p_{1/2}$ core levels for C-$LiMn_2O_4$ and E-$LiMn_2O_4$ samples. Deconvolution was performed with the binding energy positions of Mn^{3+} and Mn^{4+} ions taken at 642.1 and 643.6 eV, respectively.

Fig. 8. Cyclic voltammograms recorded at a scan rate of 0.05 mV s^{-1} in the voltage range 3.5-4.5 V vs. Li^+/Li^0 of (a) C-$LiMn_2O_4$ and (b) E-$LiMn_2O_4$.

Fig. 9. Charge–discharge curves of (a) C-$LiMn_2O_4$ and (b) E-$LiMn_2O_4$ electrode taken at 0.1C between 3.0 and 4.5 V vs. Li^+/Li^0.

Fig. 10. Cyclic performance of C-$LiMn_2O_4$ and E-$LiMn_2O_4$ samples: (a) Specific discharge capacity at various C-rates. (b) Specific discharge capacity vs. cycle number at rate 0.5 C. Both cells were cycled in the potential range 3.0-4.5 V vs. Li^+/Li^0.